Janus monolayers of magnetic transition metal dichalcogenides as an all-in-one platform for spin-orbit torque

Idris Smaili, Slimane Laref, Jose H Garcia, Udo Schwingenschlögl, Stephan Roche, Aurélien Manchon

Janus Monolayers of Magnetic Transition Metal Dichalcogenides as a Platform for Spin-Orbit Torque

Idris Smaili[1],* Slimane Laref[2],† Jose H. Garcia[3], Udo Schwingenschlögl[2], Stephan Roche[3,4], and Aurélien Manchon[1,2,5‡]
[1]*King Abdullah University of Science and Technology (KAUST), Computer, Electrical, and Mathematical Science and Engineering Division (CEMSE), Thuwal 23955-6900, Saudi Arabia*
[2]*King Abdullah University of Science and Technology (KAUST), Physical Science and Engineering Division (PSE), Thuwal 23955-6900, Saudi Arabia*
[3]*Catalan Institute of Nanoscience and Nanotechnology (ICN2), CSIC and BIST, Campus UAB, Bellaterra, 08193 Barcelona, Spain*
[4]*ICREA–Institució Catalana de Recerca i Estudis Avançats, 08010 Barcelona, Spain*
[5] *Aix-Marseille Univ, CNRS, CINaM, Marseille, France.*

We theoretically predict that vanadium-based Janus dichalcogenide monolayers constitute an ideal platform for spin-orbit torque memories. Using first principles calculations, we demonstrate that magnetic exchange and magnetic anisotropy energies are higher for heavier chalcogen atoms, while the broken inversion symmetry in the Janus form leads to the emergence of Rashba-like spin-orbit coupling. The spin-orbit torque efficiency is evaluated using optimized quantum transport methodology and found to be comparable to heavy nonmagnetic metals. The coexistence of magnetism and spin-orbit coupling in such materials with tunable Fermi-level opens new possibilities for monitoring magnetization dynamics in the perspective of non-volatile magnetic random access memories.

I. INTRODUCTION

The search for magnetism in two-dimensional (2D) materials has experienced a complete revival in recent years, with the observation of room temperature magnetism[1]. Layered van der Waals materials such as transition metal phosphorous trichalcogenides[2] ($MnPS_3$, $NiPS_3$ etc.), transition metal trihalides[3] ($CrCl_3$, CrI_3), and transition metal dichalcogenides[4] (TMDs - VSe_2, $CrSe_2$, $CrTe_2$) are all known to display quasi-two dimensional magnetism and therefore have the potential for supporting magnetism down to the monolayer limit. Remarkably, 2D magnetism has been recently reported in CrI_3[5], $CrSiTe_3$[6] and $Cr_2Ge_2Te_6$[7] mono- and bilayers, as well as in Fe_3GeTe_2[8,9], VSe_2[10], and $MnSe_2$[11] monolayers. The latter results obtained at room temperature, are particularly intriguing because TMDs are known to exhibit charge density wave instabilities, preventing the onset of magnetism[12,13]. This observation suggests that the substrate plays an important role in the stabilization of magnetism, which has yet to be confirmed experimentally. Despite this on-going debate, these discoveries open appealing perspectives for low-dimensional electronics.

In fact, among the vast zoology of 2D materials, the family of TMDs offers a versatile platform for the advancement of disruptive ultrathin electronics[14,15]. The advent of 2D magnetism fosters the realization of flat spintronic devices, whose operation is based on the electron's spin rather than its charge. For instance, tunneling magnetoresistance[16], and spin tunnel field-effect transistors[17] have been recently realized. In addition, TMDs also have a large spin-orbit coupling[18] that has been successfully exploited for gate-controlled spin manipulation in graphene/TMD bilayers[19–22]. This feature is particularly interesting in the context of spintronics as it enables the onset of spin-orbit torque[23]. Spin-orbit torque (SOT) is a mechanism by which the orbital angular momentum is transferred to the spin angular momentum via spin-orbit coupling, thereby inducing a magnetic torque of the magnetization. It requires the presence of a spin texture that is odd in momentum space, also referred to as $k-antisymmetric$ spin-momentum locking, which only emerges upon inversion symmetry breaking and spin-orbit coupling. The effect has been reported in both non-centrosymmetric magnets[24] and magnetic multilayers involving heavy transition metal[25,26] and TMD substrates[27–29], opening avenues for the development of non-volatile magnetic random access memories[30]. In this context, magnetic TMDs present an interesting paradigm for the realization of such ultrathin SOT magnetic random access memories.

In this Article, we study the so-called Janus monolayer where the transition metal ion is embedded between dissimilar chalcogen elements. Such a Janus structure has been predicted and realized experimentally in nonmagnetic TMDs[31–34]. Remarkably, the dissimilarity between the electronegativity of the two chalcogen elements induces an electric dipole perpendicular to the plane of the monolayer and promotes Rashba-type spin-orbit coupling[31,35,36], resulting in Dzyaloshinskii-Moriya exchange interaction when the transition metal element is magnetic[37–41]. In the present work, we demonstrate that such a structure constitutes a remarkable paradigm for SOT-building block. Magnetic properties of the 2H phase of vanadium-based TMDs have been previously studied by density functional theory (DFT)[42–45], but the more experimentally-relevant 1T phases remain to be explored in-depth. Our first principles calculations of various vanadium-based TMDs in their 1T phase unveil the impact of inversion symmetry breaking on the mag-

netic properties and the emergence of Rashba-like spin textures, which are key enabling features for current-driven gate-controlled SOT activation of magnetic dynamics and reversal.

II. MODELING SPIN-ORBIT TORQUE IN JANUS MONOLAYERS

A. Methodology

We consider a VXY Janus monolayer with vanadium (V) concentrating most of the magnetic moments and octahedrally coordinated with chalcogenides ions (X and Y) in the 1T-phase, as depicted on the inset of Fig. 1. The DFT calculations were performed using the Perdew-Burke-Ernzerhof (PBE) method of the generalized gradient approximation (GGA) exchange-correlation functional as implemented in the Vienna Ab initio Simulation Package[46,47] (VASP). Grimme dispersion correction with Becke-Jonson damping (DFT-D3) has been adopted to eliminate the effect of van der Waals interactions[48,49]. In the calculations, an energy cutoff of 600 eV is used for the plane-wave basis expansion, and total energies are properly converged with criteria of 10^{-5} eV per unit cell. Γ-centered k-grids 10×10×1, 16×16×1, 24×24×1, and 32×32×1 have been sampled for the structural and magnetic calculations. A vacuum space of 15 Å has been applied to avoid interaction between monolayers. The magnetic configuration has been assessed based on the force theorem by computing $J = E_{\mathrm{AFM}} - E_{\mathrm{FM}}$, where E_{AFM} and E_{FM} represent the total energies for the simple (G-type) antiferromagnetic and ferromagnetic spin arrangements, respectively. Spin texture calculations of the valence band of 1T-VXY monolayers have been investigated around the Γ point and for the [001] orientation for model systems of 1×1 boxes within three atomic layers of 1T-VXY. Crystal structures of the bulk VXY have been optimized by establishing the ground state geometries. The phonon band structure is computed using density functional perturbation theory (DFPT) implemented in Phonopy[50]. To obtain the constants of forces, we used $2 \times 2 \times 1$ monolayers.

The SOT efficiency is computed in the linear-response regime by using the Kubo-Bastin formula[51]

$$\langle \hat{A}(\varepsilon) \rangle = -2 \int_{-\infty}^{\varepsilon} d\varepsilon' \mathrm{Im} \left(\mathrm{tr} \left[\delta(\varepsilon' - \hat{H}) \hat{A} \partial_{\varepsilon'} G^{+}_{\varepsilon'} (\hat{\boldsymbol{J}} \cdot \boldsymbol{E}) \right] \right), \tag{1}$$

where $\hat{A}$ is the operator driven out of equilibrium by the electric field $\boldsymbol{E}$, $\hat{\boldsymbol{J}}$ the current operator which can be expressed in terms of the Hamiltonian $\hat{H}$ and the position operator $\hat{\boldsymbol{R}}$ as $\hat{\boldsymbol{J}} \equiv -e[\hat{H}, \hat{\boldsymbol{R}}]$, and $G^{+}_{\varepsilon} \equiv \lim_{\eta \to 0} 1/(\hat{H} - \varepsilon + i\eta)$ is the retarded Green's function. For the spin density, we used $\hat{A} \to \hat{\boldsymbol{S}} = \frac{1}{\Omega} \sum_i \hat{c}_i^{\dagger} \hat{\boldsymbol{\sigma}} \hat{c}_i$ where $\hat{c}_i^{\dagger} = (c_{i,\uparrow}^{\dagger}, c_{i,\downarrow}^{\dagger})$ and $\hat{\boldsymbol{\sigma}}$ is the vector of Pauli matrices for spin 1/2. The torque is computed by $\hat{A} \to \hat{\boldsymbol{\tau}} = \frac{1}{\Omega} \mathbf{m} \times \sum_i \Delta_i \hat{c}_i^{\dagger} \hat{\boldsymbol{\sigma}} \hat{c}_i$, Δ_i being the s-d exchange on the ith orbital. The Green's functions in the Kubo-Bastin formula are approximated numerically by using the Kernel Polynomial Method[52–54] using 300 Chebyshev expansion moments, which is equivalent to a broadening of 54 meV for this particular system. The calculations were performed on a multiorbital tight-binding Hamiltonian by projecting the band structure on maximally-localized Wannier functions as implemented in WANNIER90[55]. The system was then expanded into a 40×40 supercell, which amounts to 35200 orbitals in the case of VSeTe.

TABLE I. Magnetic properties extracted from fully relativistic first principles methods of selected vanadium-based T-VXY

Material	E_{A} (meV)	J (meV)	μ_{s} (μ_{B})	S (μ_{B})	L (μ_{B})
VTe_2	0.239	38.96	1.454	1.476	-0.025
VTeSe	0.241	50.82	1.362	1.391	-0.024

B. Magnetic properties

We compute the magnetic properties of the full vanadium-based TMD series and found ferromagnetic order ground states for all elements. In Table I, we report the magnetic properties of monolayers involving Te, which were the only one displaying a finite magnetic anisotropy energy (E_{A}) together with the largest exchange energies (J) and magnetic moment (μ_{s}), dominated by the spin contribution (S). Remarkably, VTe_2 and VSeTe also possess the largest orbital angular momentum (L), which is a precursor for the formation of a Rashba-like spin-momentum locking in the Janus form.

Figure 1 shows the effect of chalcogen substitution where it is clear that lighter atoms are detrimental to the magnetic and orbital properties, suppressing the magnetic anisotropy, and reducing the exchange energy, magnetic moment and orbital momentum altogether. We found that such a behavior is associated with a depletion of the charge density on vanadium due to ionic bonding with the chalcogen elements, which is larger for sulfur chalclogen as we demonstrated by performing a Bader charge analysis (e_{B} in Fig. 1). In addition, these results suggest that vanadium-based chalcogenide monolayers have the capability for *easy-plane* magnetic anisotropy, which makes them an interesting platform for the realization of spin superfluidity, a remarkably efficient manner to convey spin information[56].

To confirm the structural stability of the Janus monolayers, we performed phonon band dispersion calculations. The phonon dispersion along $\Gamma - M - K - \Gamma$ direction are reported on Fig. 2. In these calculations, negative modes around symmetry points, i.e. Γ, M, and

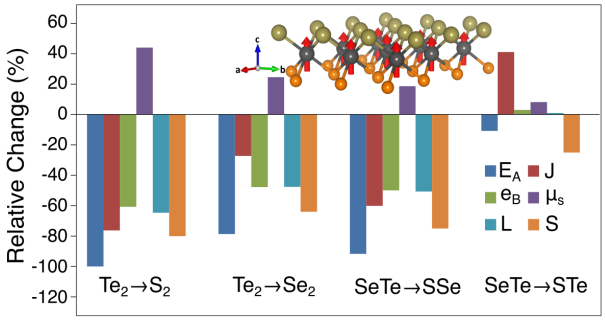

FIG. 1. (Color Online) Relative changes of the magnetic anisotropy E_A, exchange coupling J, magnetic moment μ_s, Bader charge e_B and orbital angular momentum L in VTe_2 upon substitution of Te atoms by sulfur (S) and selenium (Se), and also upon the transformation from the Janus form VSeTe into VSSe and VSeTe.

K, usually indicate a structural instability. However, neglecting force constants symmetrization can cause negative frequencies around Γ point and therefore, such negative frequencies are considered meaningless in Phonopy calculations[50,57]. Consequently, Fig. 2 confirm that the magnetic Janus TMDs studied in this work are structurally stable.

To identify the bonding characteristics of 1T-VXY monolayers, we compute the projected densities of states for all magnetic TMDs around the Fermi level. We determined that the contributions of the p-orbitals of the chalcogens and the d-orbitals of vanadium dominate around the Fermi level, whereas the other orbitals have negligible contributions, as seen in Fig. 3(a) for VTe_2 and Fig. 3(b) for VSeTe. Such a result indicates that the states around the Fermi level are due to a covalent hybridization of the vanadium d-orbitals with the p-orbitals of the chalcogens. Interestingly, the density of states for down spins (negative values) is substantially reduced around Fermi energy, implying that the magnetic TMDs are in fact close to half-metallic behavior.

We will now focus on understanding the role of the broken inversion symmetry, which reduces the point group symmetry from D_{3d} to C_{3v}. For both groups, the d-orbitals split into three states, a (d_{z^2}) state, and two twofold degenerate states (d_{zx}, d_{yz}) and ($d_{x^2-y^2}$, d_{xy}). In Fig. 3(b,d), we show the density of states projected on these five d orbitals, where it is clear that (d_{zx}, d_{yz}) is strongly suppressed around the Fermi energy, while ($d_{x^2-y^2}$, d_{xy}) are ubiquitous. Such an imbalance between the degenerate orbitals at the Fermi energy is directly associated with the emergence of a large orbital moment, and explains why Te has the largest orbital moment when compared to the other chalcogens (see Fig. 1). The (d_{z^2}) state is a consequence of p-d hybridization, hence it is strongly suppressed in VTe_2 [Fig. 3(b)] but is significant in VSeTe due to the broken inversion symmetry [Fig. 3(d)]. The enhanced orbital moment and p-d hybridization suggests the formation of a Rashba-like spin-momentum locking.

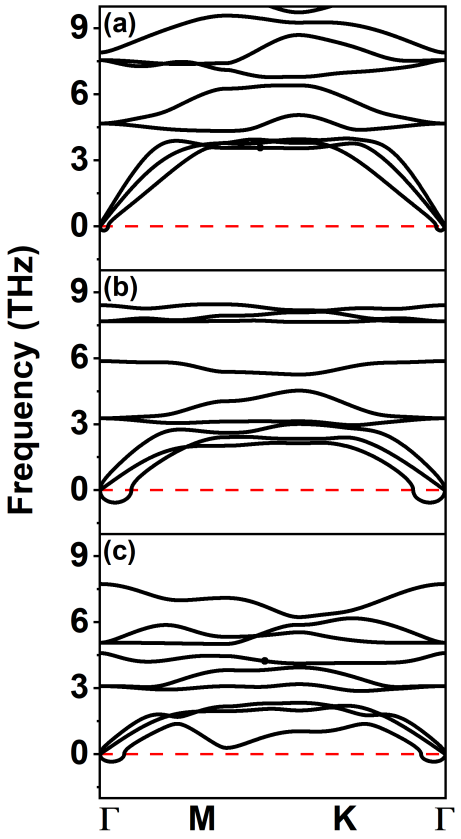

FIG. 2. (Color Online) Phonon band diagrams of (a) VSSe, (b) VSTe, and (c) VSeTe monolayers.

C. Rashba-like spin-momentum locking

To determine how the inversion asymmetry promotes k-antisymmetric spin-momentum locking in VSeTe, we compute its spin-projected band structure along M-Γ-M, see Fig. 4. The band structure is then projected on the spin components of p-orbitals of Se (a) and Te (b), as well as on that of d-orbitals of V (c). The bottom band possesses both p and d characters, while the top band is dominated by Se p orbitals. These Se p orbitals exhibit spin polarization along the magnetization direction, S_z, [right subpanel in Fig. 4(a)], and most importantly, an in-plane spin density S_x that is antisymmetric in momentum k. This antisymmetric feature is the fingerprint of Rashba-like spin-momentum locking[58]. However, because it is carried by the chalcogen elements that are weakly magnetized, this odd-in-k spin-orbit coupling does not allow for current-driven spin-orbit torque.

Fig. 4(c) shows that d orbitals are present all across the band structure, displaying strong spin-polarization and even near half-metallicity [right subpanel in Fig. 4(c)]. The most important feature though is the Rashba-

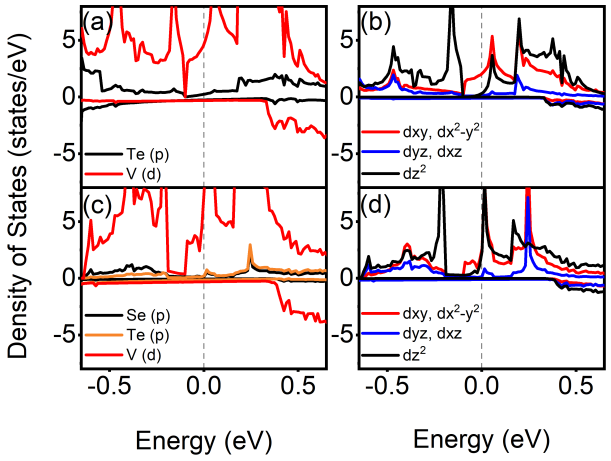

FIG. 3. (Color Online) Projected density of states of (a,b) VTe_2 and (c,d) VSeTe. The left panels display the projection of Se-p, Te-p and V-d orbitals, whereas the right panels display the orbital-resolved projection on the V-d orbitals. Positive (negative) density of states stands for up (down) spins.

like spin-momentum locking displayed by the bottom band. This spin-momentum locking, being antisymmetric in k and carried by a magnetic band, enables current-driven spin-orbit torques. For completeness, we also report the S_x component of the spin texture in momentum space projected on (d) p-Se orbitals, (e) p-Te orbitals and (f) d-V orbitals at Fermi level. Close to Γ-point, the Fermi surface is circular and hexagonal warping appears further away. Notice though that the spin-momentum locking of the two central Fermi contours is much stronger than that of the external one.

We develop a minimal model to understand the physical origin of spin-momentum locking in Janus monolayers. We first analyse the nature of the orbital hybridization by computing the Kohn-Sham orbitals at Fermi level for (a) 1T-VSe_2, (b) 1T-VTe_2 and (c) 1T-VSeTe, shown in Fig. 5. This figure indicates that the hybridization is dominated by the d_{z^2} orbital from vanadium and p_z orbitals from Selenium. Therefore, a minimal tight-binding model should primarily account for this hybridization. In addition, looking at the spin-orbit coupling matrix, $\mathcal{H}_{\rm so} = \xi_{\rm so}\mathbf{L}\cdot\mathbf{S}$ for d orbitals, the only way to obtain in-plane spin component is to hybridize d_{z^2} and (d_{zx}, d_{yz}) orbitals [see Fig. 6(d)]. Since the magnetic band obtained in Fig. 4(c) is dominated by d_{z^2} orbitals, we will develop a perturbation theory of the d_{z^2} band under the hybridization with p_z orbitals. This hybridization is expected to induce an admixture of d_{z^2} and (d_{zx}, d_{yz}) orbitals at the second order, which produces the Rashba-like spin-orbit interaction. The minimal model is sketched in Fig. 6(a,b,c).

Point group analysis implies that the degenerate orbitals (d_{zx}, d_{yz}) only appear in $|s\rangle = |d_{yz}\rangle \pm i|d_{zx}\rangle$ combinations. Therefore, the second order perturbation of the d_{z^2} orbital gives

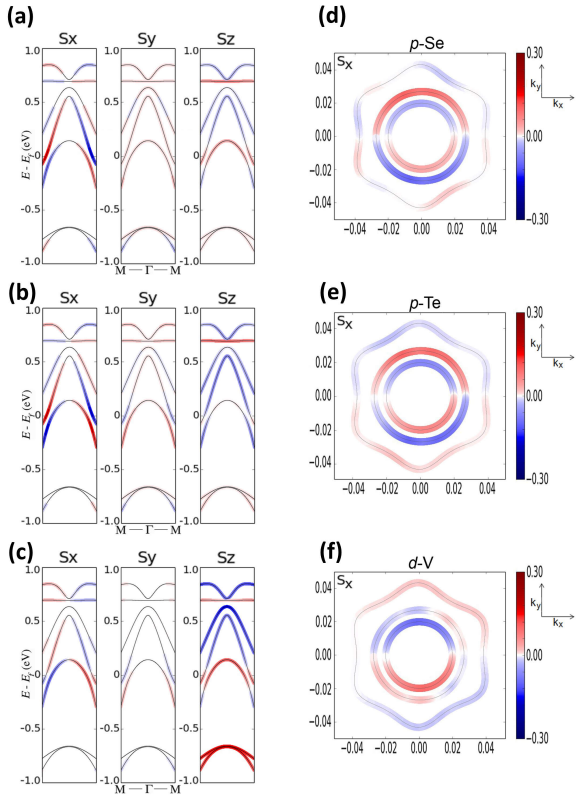

FIG. 4. (Color Online) Left panels: spin-resolved band structure of 1T-VSeTe projected on (a) p-Se orbitals, (b) p-Te orbitals and (c) d-V orbitals. The three subpanels refer to S_x, S_y and S_z components of the spin density, the red (blue) color indicates a positive (negative) value. Right panels: S_x component of the spin texture in momentum space projected on (d) p-Se orbitals, (e) p-Te orbitals and (f) d-V orbitals. During these calculations, the magnetization is set perpendicular to the plane.

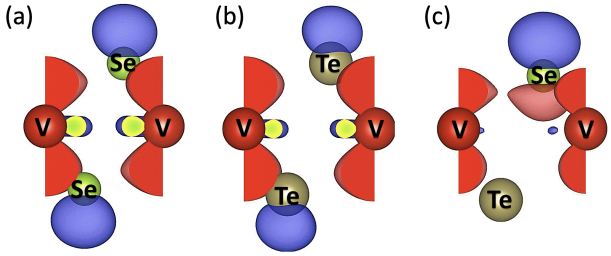

FIG. 5. (Color Online) Orbital hybridization: Kohn-Sham orbitals of (a) 1T-VSe_2, (b) 1T-VTe_2 and (c) 1T-VSeTe.

$$|d_{z^2}\rangle_p = \left(1 - \frac{1}{2}\sum_{\alpha}\frac{|V^{\alpha}_{z^2,z}|^2}{(\varepsilon_{d_{z^2}} - \varepsilon_{\alpha})^2}\right)|d_{z^2}\rangle_0 + \sum_{s,\alpha}\frac{V^{\alpha}_{s,z}V^{\alpha}_{z,z^2}}{(\varepsilon_{d_{z^2}} - \varepsilon_s)(\varepsilon_{d_{z^2}} - \varepsilon_{\alpha})}|s\rangle_0. \quad (2)$$

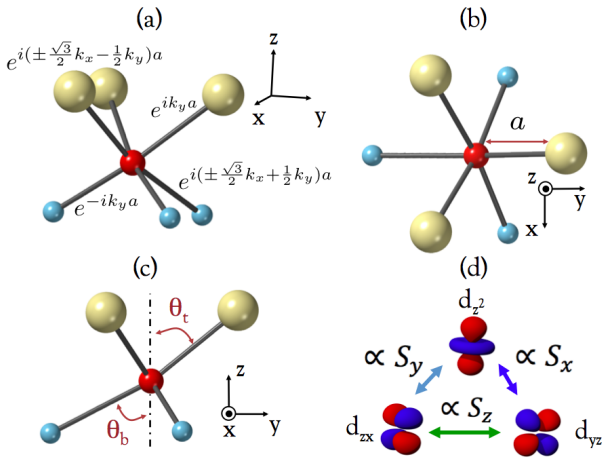

FIG. 6. (Color Online) (a) Schematics of the tight-binding model of a Janus monolayer with vanadium (red) surrounded by dissimilar chalcogens (yellow and blue). The phases acquired by the electron Bloch state when hopping from vanadium to the chalcogen element are given. (b) View of the model in the (x,y) plane and (c) in the (y,z) plane. In the latter the angles formed by the top and bottom bonds with **z** are given. (d) Representation of the spin-orbit coupling scheme between the three d-orbitals considered in the model.

Here, $V^{\alpha}_{z^2,z}$ ($V^{\alpha}_{s,z}$) is the hopping integral between d_{z^2} (s) and p_z orbital from chalcogen α and ε_η is the energy of orbital η. The hopping parameters are computed within the two-center Slater-Koster approximation[59] and read $V^{\alpha}_{\eta,z} = V^{\alpha}_{\eta} f^{\alpha}_{\eta}$, with

$$V^{\alpha}_{z^2} = \left[\frac{1}{2}(3\cos^2\theta_\alpha - 1)V^{\alpha}_{\sigma} + \sqrt{3}V^{\alpha}_{\pi}\sin^2\theta_\alpha\right]\cos\theta_\alpha f_{z^2},$$
$$V^{\alpha}_{s} = \left[\sqrt{3}\cos^2\theta_\alpha V^{\alpha}_{\sigma} + (1-2\cos^2\theta_\alpha)V^{\alpha}_{\pi}\right]\sin\theta_\alpha f_{s},$$
$$f^{\alpha}_{z^2} = e^{ik_y\frac{a_0}{\sqrt{3}}} + 2\cos\left(k_x\frac{a_0}{2}\right)e^{-ik_y\frac{a_0}{2\sqrt{3}}},$$
$$f^{\alpha}_{s} = e^{ik_y\frac{a_0}{\sqrt{3}}} - \cos\left(k_x\frac{a_0}{2} + s\frac{\pi}{3}\right)e^{-ik_y\frac{a_0}{2\sqrt{3}}}.$$

We are looking for the spin-orbit coupling energy $\mathcal{H}_{\rm so}$ of this perturbed state, which gives

$$\langle d_{z^2}|\mathcal{H}_{\rm so}|d_{z^2}\rangle_p = 2{\rm Re}\left[\frac{V^{\alpha}_{z^2,z}V^{\alpha}_{z,s}\langle s|\mathcal{H}_{\rm so}|d_{z^2}\rangle}{(\varepsilon_{z^2}-\varepsilon^{\alpha}_{p_z})(\varepsilon_{z^2}-\varepsilon_s)}\right].$$

Close to Γ-point, we obtain

$$\langle d_{z^2}|\mathbf{L}\cdot\mathbf{S}|d_{z^2}\rangle_p \approx \alpha_{\rm R}\hat{\boldsymbol{\sigma}}\cdot(\mathbf{z}\times\mathbf{k}) \tag{3}$$

where

$$\alpha_{\rm R} = 18\xi_{\rm so}a_0\sum_{\alpha}\left[\frac{V^{\alpha}_{s}V^{\alpha}_{z^2}}{(\varepsilon_{z^2}-\varepsilon^{\alpha}_{p_z})(\varepsilon_{z^2}-\varepsilon_s)}\right] \tag{4}$$

This expression demonstrates that coupling the d-orbitals of vanadium with dissymmetric chalcogen bonding induces Rashba spin-orbit coupling close to Γ point, in agreement with the first principle calculations discussed above. The large spin splitting implies that only one spin chirality contributes to the spin transport, making this systems optimal for SOT.

D. Spin-orbit torque simulations

After establishing the formation of Rashba-like spin-texture coupled to the magnetic moments in the Janus structure, we now evaluate its impact on the SOT efficiency. By considering the C_{3v} symmetry of the Janus monolayer and applying the Neumann's principle to the current-driven field tensor[60], one determines that the torque possesses two components,

$$H_{\rm FL} = \chi_{\rm FL}\mathbf{z}\times\mathbf{E} \tag{5}$$
$$H_{\rm DL} = \chi^1_{\rm DL}\mathbf{m}\times(\mathbf{z}\times\mathbf{E}) + \chi^2_{\rm DL}m_z\mathbf{E} + \chi^2_{\rm DL}[(m_yE_x + m_xE_y)\mathbf{x} + (m_xE_x - m_yE_y)\mathbf{y}]. \tag{6}$$

The first terms ($\chi_{\rm FL}, \chi^1_{\rm DL}$) are similar to the one expected from the standard theory of the Rashba gas, while the third damping-like term ($\chi^2_{\rm DL}$) arises from the threefold rotation combined with the mirror symmetry. A similar term was obtained by Johansen *et al.*[61] for Fe_3GeTe_2, and one can show that it derives from a potential $E_{\rm T} = \chi^2_{\rm DL}(m_xm_yE_x + (m^2_x - m^2_y)E_y/2)$, which therefore expresses a current-driven magnetic anisotropy[61,62]. Importantly, in contrast to Fe_3GeTe_2, the obtained torque in 1T-VSeTe coexists with the conventional "Rashba" torques and therefore has the ability to modify the overall magnetization dynamics and even permits *zero-field switching*. The zero-field switching arising from the cooperation between the current-driven magnetic anisotropy and the damping-like torque was demonstrated experimentally in a CuPt/CoPt $L1_1$ crystalline bilayer that adopts C_{3v} symmetry[63]. In a realistic system though, this zero-field switching torque arises from Bloch states experiencing the C_{3v} crystal field, so for states typically lying *away* from Γ-point. In vanadium dichalcogenides, the magnetic and transport properties are dominated by states close to Γ-point [Fig. 4(b)], which suggests that these properties shall display cylindrical symmetry at the lowest order, and that high-order effects, such as the derived current-driven magnetic anisotropy or the threefold magnetocrystalline anisotropy expected in hexagonal magnets, should only emerge as a small correction. As a matter of fact, our calculation of the magnetic anisotropy cannot resolve any threefold planar component, so that the value of $\chi^2_{\rm DL}$ should be vanishingly small.

Figure 7 shows the energy dependence of the torque efficiency when the magnetization points out of plane (τ_z - top) and in the plane ($\tau_\perp$ - bottom), computed by setting the electric field along **x**. We verified that similar results are obtained when setting the electric field along **y**. The torque efficiency is defined as the torque per unit electric field divided by the longitudinal conductivity, $\chi_{\rm FL,DL}/\sigma_c$, and is unitless. We find that the

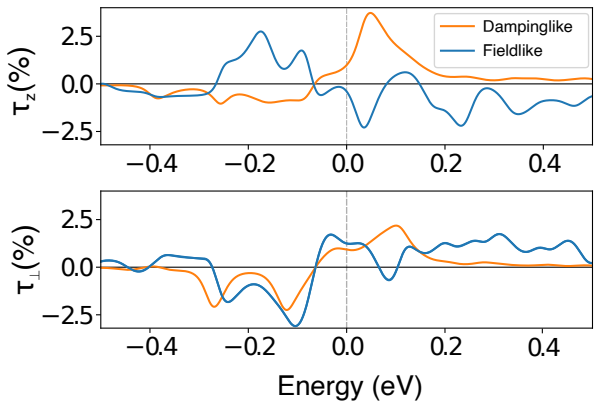

FIG. 7. (Color Online) Current-driven torque efficiency as a function of the transport energy, when the magnetization lies perpendicular to the plane (top) and in plane (bottom). The figure shows both the dampinglike (orange) and fieldlike (blue) components.

torque adopts the conventional Rashba form, Eqs. (5)-(6), displaying both dampinglike (orange) and fieldlike torques (blue) with a strong anisotropy when changing the magnetization direction from in-plane to out-of-plane. Additional components with one order of magnitude smaller than the conventional torques are observed and discarded. Although the overall magnitude of the torque ($\tau_{z,\perp} < 2.5$ %) remains limited compared to the best transition metal substrates[23] such as Pt (~ 8 %) and W (~ 30 %), we emphasize that it is surprisingly large when considering the smallness of the atomic spin-orbit coupling of V (∼20 meV) compared to that of Pt (∼400 meV)[64].

Let us now determine that the current density required to overcome VSeTe anisotropy. VSeTe possesses both a large magnetic moment (μ_s =4.58 μ_B, corresponding to $M_s \approx 1.34 \times 10^6$ A/m) and a large planar anisotropy ($K = 0.24$ meV, corresponding to $\mu_0 H_\perp = 2K/\mu_s \approx 1.8$ T). Assuming the existence of an in-plane uniaxial anisotropy (e.g., induced by the substrate), $\mu_0 H_a \ll \mu_0 H_\perp, \mu_0 M_s$ (typically, $\mu_0 H_a \approx 10-50$ mT), the current density required to overcome this anisotropy is[26]

$$J_c^0 = \left(\frac{2e}{\hbar}\right) \frac{\alpha}{\tau_s} \mu_0 M_s d \left(H_a + H_\perp/2 + 2\pi M_s\right), \qquad (7)$$

where $\tau_s = \chi_{\rm DL}/\sigma_c$ is the torque efficiency. At zero temperature, taking $\tau_s = 0.02$, $\alpha = 0.01$, d=3.093Å, we obtain a critical current of $J_c^0 \approx 7.5 \times 10^7$ A/cm^2. Notice that J_c^0 has been computed at zero temperature and will be naturally further reduced by thermal activation under experimental conditions. Another remarkable feature is the possibility to *quench* the magnitude of the torque by tuning the Fermi level. Indeed, Fig. 7 shows that τ_z ($\tau_\perp$) is maximum around 50 meV (-100 meV) from Fermi level. As a result, by tuning the Fermi level either by doping or using the more technologically relevant ionic gate voltage control, one can substantially enhance the efficiency of the torque and turn it on and off at will, thereby implementing a *gate-controlled spin switch*. Interestingly, the magnetic properties of 2D materials are highly sensitive to surface engineering and substrate effects, enabling versatile tuning of the magnetic anisotropy[65,66].

III. CONCLUSION

We studied monolayers vanadium-bases magnetic TMDs in their Janus form as *all-in-one* SOT building block, allowing for electrically-controlled magnetism in a single material. Among the different candidates, we found that VSeTe is the most promising due to possessing the largest magnetic anisotropy, exchange interaction, and Rashba-like behavior. We evaluated how these features translate into the magnetization dynamics by computing the current-driven torque using Kubo formula and demonstrated that it is large enough to realize switching at room temperature. Moreover, we also show that such a switching can be tuned by electronic or ionic gating, opening fascinating perspectives for applications such as SOT magnetic memories and spin-charge conversion devices.

ACKNOWLEDGMENTS

The authors were supported by King Abdullah University of Science and Technology (KAUST) through the award OSR-2018-CRG7-3717 from the Office of Sponsored Research (OSR). For computer time, this research used the resources of the Supercomputing Laboratory at KAUST. ICN2 authors were supported by the European Union Horizon 2020 research and innovation programme under Grant Agreement No. 881603 (Graphene Flagship), by the CERCA Programme/Generalitat de Catalunya, and by the Severo Ochoa program from Spanish MINECO (Grant No. SEV-2017-0706 and MAT2016-75952-R).

* idris.smaili@kaust.edu.sa
† slimane.laref@kaust.edu.sa
‡ aurelien.manchon@kaust.edu.sa

[1] C. Gong and X. Zhang, Science **363**, 706 (2019).
[2] P. A. Joy and S. Vasudevan, Physical Review B **46**, 5425 (1992).
[3] M. A. McGuire, G. Clark, S. KC, W. M. Chance, G. E. Jellison, V. R. Cooper, X. Xu, and B. C. Sales, Physical

Review Materials **1**, 014001 (2017).
[4] D. C. Freitas, R. Weht, A. Sulpice, G. Remenyi, P. Strobel, F. Gay, J. Marcus, and M. Núñez-Regueiro, Journal of Physics Condensed Matter **27**, 176002 (2015).
[5] B. Huang, G. Clark, E. Navarro-Moratalla, D. R. Klein, R. Cheng, K. L. Seyler, D. Zhong, E. Schmidgall, M. A. McGuire, D. H. Cobden, W. Yao, D. Xiao, P. Jarillo-Herrero, and X. Xu, Nature **546**, 270 (2017).
[6] W. Lin, K. Chen, S. Zhang, and C. L. Chien, Physical Review Letters **116**, 186601 (2016), arXiv:1603.00931.
[7] C. Gong, L. Li, Z. Li, H. Ji, A. Stern, Y. Xia, T. Cao, W. Bao, C. Wang, Y. Wang, Z. Q. Qiu, R. J. Cava, S. G. Louie, J. Xia, and X. Zhang, Nature **546**, 265 (2017).
[8] Z. Fei, B. Huang, P. Malinowski, W. Wang, T. Song, J. Sanchez, W. Yao, D. Xiao, X. Zhu, A. F. May, W. Wu, D. H. Cobden, J.-h. Chu, and X. Xu, Nature Materials **17**, 778 (2018).
[9] Y. Deng, Y. Yu, Y. Song, J. Zhang, N. Z. Wang, Z. Sun, and Y. Yi, Nature **563**, 94 (2018).
[10] M. Bonilla, S. Kolekar, Y. Ma, H. C. Diaz, V. Kalappattil, R. Das, T. Eggers, H. R. Gutierrez, M.-H. Phan, and M. Batzill, Nature Nanotechnology **13**, 289 (2018).
[11] D. J. O'Hara, T. Zhu, A. H. Trout, A. S. Ahmed, Y. K. Luo, C. H. Lee, M. R. Brenner, S. Rajan, J. A. Gupta, D. W. McComb, and R. K. Kawakami, Nano Letters , acs.nanolett.8b00683 (2018), arXiv:1802.08152.
[12] M. B. Walker and R. L. Withers, Physical Review B **28**, 2766 (1983).
[13] P. M. Coelho, K. N. Cong, M. Bonilla, S. Kolekar, M.-h. Phan, J. Avila, M. C. Asensio, I. I. Oleynik, and M. Batzill, The Journal of Chemical Physics **123**, 14089 (2019).
[14] X. Xu, W. Yao, D. Xiao, and T. F. Heinz, Nature Physics **10**, 343 (2014).
[15] M.-Y. Li, S.-K. Su, H.-S. P. Wong, and L.-J. Li, Nature **567**, 170 (2019).
[16] T. Song, X. Cai, M. W.-y. Tu, X. Zhang, B. Huang, N. P. Wilson, K. L. Seyler, L. Zhu, T. Taniguchi, K. Watanabe, M. A. Mcguire, D. H. Cobden, and D. Xiao, Science (New York, N.Y.) **360**, 1214 (2018).
[17] S. Jiang, L. Li, Z. Wang, J. Shan, and K. F. Mak, Nature Electronics **2**, 159 (2019).
[18] Z. Y. Zhu, Y. C. Cheng, and U. Schwingenschlögl, Physical Review B **84**, 153402 (2011).
[19] W. Yan, O. Txoperena, R. Llopis, H. Dery, L. E. Hueso, and F. Casanova, Nature Communications **7**, 13372 (2016).
[20] A. Dankert and S. P. Dash, Nature Communications **8**, 16093 (2017).
[21] T. S. Ghiasi, A. A. Kaverzin, P. J. Blah, and B. J. van Wees, Nano Lett. **19**, 5959 (2019).
[22] L. A. Benítez, W. Savero Torres, J. F. Sierra, M. Timmermans, J. H. Garcia, S. Roche, M. V. Costache, and S. O. Valenzuela, Nature Materials **19**, 170 (2020).
[23] A. Manchon, J. Železný, M. Miron, T. Jungwirth, J. Sinova, A. Thiaville, K. Garello, and P. Gambardella, Review of Modern Physics **91**, 035004 (2019).
[24] A. Chernyshov, M. Overby, X. Liu, J. K. Furdyna, Y. Lyanda-Geller, and L. P. Rokhinson, Nature Physics **5**, 656 (2009).
[25] I. M. Miron, K. Garello, G. Gaudin, P. J. Zermatten, M. V. Costache, S. Auffret, S. Bandiera, B. Rodmacq, A. Schuhl, and P. Gambardella, Nature **476**, 189 (2011).
[26] L. Liu, C.-F. Pai, Y. Li, H. W. Tseng, D. C. Ralph, and R. A. Buhrman, Science **336**, 555 (2012).
[27] Q. Shao, G. Yu, Y.-w. Lan, Y. Shi, M.-Y. Li, C. Zheng, X. Zhu, L.-J. Li, P. K. Amiri, and K. L. Wang, Nano Letters **16**, 7514 (2016).
[28] D. MacNeill, G. M. Stiehl, M. H. D. Guimaraes, R. A. Buhrman, J. Park, and D. C. Ralph, Nature Physics **13**, 300 (2017).
[29] G. M. Stiehl, D. Macneill, N. Sivadas, I. E. Baggari, M. H. D. Guimara, N. D. Reynolds, L. F. Kourkoutis, C. J. Fennie, R. A. Buhrman, and D. C. Ralph, ACS Nano **13**, 2599 (2019).
[30] M. Cubukcu, O. Boulle, N. Mikuszeit, C. Hamelin, T. Bräcker, N. Lamard, M.-C. Cyrille, L. Buda-Prejbeanu, K. Garello, I. M. Miron, O. Klein, G. de Loubens, V. V. Naletov, J. Langer, B. Ocker, P. Gambardella, and G. Gaudin, IEEE Transactions on Magnetics **54**, 9300204 (2015), arXiv:1509.02375.
[31] Y. C. Cheng, Z. Y. Zhu, M. Tahir, and U. Schwingenschlögl, Europhysics Letters **102**, 57001 (2013).
[32] A.-y. Lu, H. Zhu, J. Xiao, C.-p. Chuu, Y. Han, M.-h. Chiu, C.-c. Cheng, C.-w. Yang, K.-h. Wei, Y. Yang, Y. Wang, D. Sokaras, D. Nordlund, P. Yang, D. A. Muller, and M.-y. Chou, Nature Nanotechnology **12**, 744 (2017).
[33] J. Zhang, S. Jia, I. Kholmanov, L. Dong, D. Er, W. Chen, and H. Guo, ACS Nano **11**, 8192 (2017).
[34] L. Zhang, Z. Yang, T. Gong, R. Pan, and H. Wang, Journal of Materials Chemistry A **8**, 8813 (2020).
[35] H. U. Din, M. Idrees, A. Albar, M. Shafiq, I. Ahmad, C. V. Nguyen, and B. Amin, Physical Review B **100**, 165425 (2019).
[36] J. Chen, K. Wu, H. Ma, W. Hu, and J. Yang, RSC Advances **10**, 6388 (2020).
[37] J. Liang, W. Wang, H. Du, A. Hallal, K. Garcia, M. Chshiev, A. Fert, and H. Yang, Physical Review B **101**, 184401 (2020), arXiv:1906.00648.
[38] F. Zhang, H. Zhang, W. Mi, and X. Wang, Phys. Chem. Chem. Phys. **22**, 8647 (2020).
[39] J. Yuan, Y. Yang, Y. Cai, Y. Wu, Y. Chen, X. Yan, and L. Shen, Physical Review B **101**, 094420 (2020).
[40] Y. Zhang, C. Xu, P. Chen, Y. Nahas, S. Prokhorenko, and L. Bellaiche, Physical Review B **102**, 241107(R) (2020).
[41] C. Xu, J. Feng, H. Xiang, and L. Bellaiche, Physical Review B **101**, 060404(R) (2020), arXiv:1906.04336.
[42] Y. Ma, Y. Dai, M. Guo, C. Niu, Y. Zhu, and B. Huang, ACS Nano **6**, 1695 (2012).
[43] H.-r. Fuh, C.-r. Chang, Y.-k. Wang, R. F. L. Evans, and R. W. Chantrell, Scientific Reports **6**, 32625 (2016).
[44] H.-r. Fuh, B. Yan, S.-c. Wu, C. Felser, and C.-r. Chang, New Journal of Physics **18**, 113038 (2016).
[45] J. He and S. Li, Computational Materials Science **152**, 151 (2018).
[46] G. Kresse and J. Hafner, Physical Review B **47**, 558 (1993).
[47] G. Kresse and J. Furthmuller, Physical Review B **54**, 11169 (1996).
[48] S. Grimme, J. Antony, S. Ehrlich, and H. Krieg, The Journal of Chemical Physics **132**, 154104 (2010).
[49] S. Grimme, WIREs Computational Molecular Science **1**, 211 (2011).
[50] A. Togo and I. Tanaka, Scripta Materialia **108**, 1 (2015).
[51] A. Bastin, C. Lewiner, O. Betbeder-Matibet, and P. Nozieres, J. Phy. Chem. Solids **32**, 1811 (1971).
[52] J. H. García, L. Covaci, and T. G. Rappoport, Physical Review Letters **114**, 116602 (2015), arXiv:1410.8140v2.
[53] J. H. Garcia, M. Vila, and A. W. Cummings, Chemical Society Reviews **47**, 3359 (2018).

[54] Z. Fan, J. H. Garcia, A. W. Cummings, J.-e. B. Vargas, A. Harju, F. Ortmann, and S. Roche, Physics Reports **903**, 1 (2021).
[55] A. A. Mostofi, J. R. Yates, G. Pizzi, Y.-s. Lee, I. Souza, D. Vanderbilt, and N. Marzari, Computer Physics Communications **185**, 2309 (2014).
[56] S. Takei and Y. Tserkovnyak, Phys. Rev. Lett. **112**, 227201 (2014).
[57] J. Skelton, "Phonons and phonopy:"pro tips"," (2015).
[58] A. Manchon, H. C. Koo, J. Nitta, S. M. Frolov, and R. A. Duine, Nature Materials **14**, 871 (2015).
[59] J. C. Slater and G. F. Koster, Physical Review **94**, 1498 (1954).
[60] J. Železný, H. Gao, A. Manchon, F. Freimuth, Y. Mokrousov, J. Zemen, J. Mašek, J. Sinova, and T. Jungwirth, Physical Review B **95**, 014403 (2017).
[61] Ø. Johansen, V. Risinggård, A. Sudbø, J. Linder, and A. Brataas, Physical Review Letters **122**, 217203 (2019).
[62] K. Zhang, S. Han, Y. Lee, M. J. Coak, J. Kim, I. Hwang, S. Son, J. Shin, M. Lim, D. Jo, K. Kim, D. Kim, H. W. Lee, and J. G. Park, Advanced Materials **33**, 2004110 (2021).
[63] L. Liu, C. Zhou, X. Shu, C. Li, T. Zhao, W. Lin, J. Deng, Q. Xie, S. Chen, J. Zhou, R. Guo, H. Wang, J. Yu, S. Shi, P. Yang, S. Pennycook, A. Manchon, and J. Chen, Nature Nanotechnology **16**, 227 (2021).
[64] S. Koseki, N. Matsunaga, T. Asada, M. W. Schmidt, and M. S. Gordon, Journal of Physical Chemistry A **123**, 2325 (2019).
[65] S. Y. Park, D. S. Kim, Y. Liu, J. Hwang, Y. Kim, W. Kim, J.-y. Kim, C. Petrovic, C. Hwang, S.-k. Mo, H.-j. Kim, B.-c. Min, H. C. Koo, J. Chang, C. Jang, J. W. Choi, and H. Ryu, Nano Letters **20**, 95 (2020).
[66] J. Kim, K.-w. Kim, B. Kim, C.-j. Kang, D. Shin, S.-h. Lee, B.-c. Min, and N. Park, Nano Letters **20**, 929 (2020).